doi:10.1093/brain/awz326 BRAIN 2019: 0; 1–16 | 1

BRAIN
A JOURNAL OF NEUROLOGY

Biallelic *DMXL2* mutations impair autophagy and cause Ohtahara syndrome with progressive course

Alessandro Esposito,[1,2,*] Antonio Falace,[3,*] Matias Wagner,[4,5,6,*] Moran Gal,[7,*] Davide Mei,[3,*] Valerio Conti,[3] Tiziana Pisano,[3] Davide Aprile,[2] Maria Sabina Cerullo,[1,2] Antonio De Fusco,[1,2] Silvia Giovedì,[2] Annette Seibt,[8] Daniella Magen,[9,10] Tilman Polster,[11] Ayelet Eran,[9,12] Sarah L. Stenton,[4,5] Chiara Fiorillo,[13,14] Sarit Ravid,[9,15] Ertan Mayatepek,[8] Hava Hafner,[9,16] Saskia Wortmann,[4,5,17] Erez Y. Levanon,[7] Carla Marini,[3] Hanna Mandel,[9,18,†] Fabio Benfenati,[1,19] Felix Distelmaier,[8,†] Anna Fassio[2,19,†] and Renzo Guerrini[3,20,†]

[*,†]These authors contributed equally to this work.

Ohtahara syndrome, early infantile epileptic encephalopathy with a suppression burst EEG pattern, is an aetiologically heterogeneous condition starting in the first weeks or months of life with intractable seizures and profound developmental disability. Using whole exome sequencing, we identified biallelic *DMXL2* mutations in three sibling pairs with Ohtahara syndrome, belonging to three unrelated families. Siblings in Family 1 were compound heterozygous for the c.5135C>T (p.Ala1712Val) missense substitution and the c.4478C>G (p.Ser1493*) nonsense substitution; in Family 2 were homozygous for the c.4478C>A (p.Ser1493*) nonsense substitution and in Family 3 were homozygous for the c.7518-1G>A (p.Trp2507Argfs*4) substitution. The severe developmental and epileptic encephalopathy manifested from the first day of life and was associated with deafness, mild peripheral polyneuropathy and dysmorphic features. Early brain MRI investigations in the first months of life revealed thin corpus callosum with brain hypomyelination in all. Follow-up MRI scans in three patients revealed progressive moderate brain shrinkage with leukoencephalopathy. Five patients died within the first 9 years of life and none achieved developmental, communicative or motor skills following birth. These clinical findings are consistent with a developmental brain disorder that begins in the prenatal brain, prevents neural connections from reaching the expected stages at birth, and follows a progressive course. DMXL2 is highly expressed in the brain and at synaptic terminals, regulates v-ATPase assembly and activity and participates in intracellular signalling pathways; however, its functional role is far from complete elucidation. Expression analysis in patient-derived skin fibroblasts demonstrated absence of the DMXL2 protein, revealing a loss of function phenotype. Patients' fibroblasts also exhibited an increased LysoTracker® signal associated with decreased endolysosomal markers and degradative processes. Defective endolysosomal homeostasis was accompanied by impaired autophagy, revealed by lower LC3II signal, accumulation of polyubiquitinated proteins, and autophagy receptor p62, with morphological alterations of the autolysosomal structures on electron microscopy. Altered lysosomal homeostasis and defective autophagy were recapitulated in *Dmxl2*-silenced mouse hippocampal neurons, which exhibited impaired neurite elongation and synaptic loss. Impaired lysosomal function and autophagy caused by biallelic *DMXL2* mutations affect neuronal development and synapse formation and result in Ohtahara syndrome with profound developmental impairment and reduced life expectancy.

1 Center for Synaptic Neuroscience and Technology, Istituto Italiano di Tecnologia, Genoa, Italy
2 Department of Experimental Medicine, University of Genoa, Genoa, Italy

Received February 22, 2019. Revised July 25, 2019. Accepted September 4, 2019

3 Pediatric Neurology, Neurogenetics and Neurobiology Unit and Laboratories, Children's Hospital A. Meyer-University of Florence, Florence, Italy
4 Institute of Human Genetics, Klinikum rechts der Isar, Technical University of München, Munich, Germany
5 Institute of Human Genetics, Helmholtz Zentrum München, Neuherberg, Germany
6 Institute for Neurogenomics, Helmholtz Zentrum München, Neuherberg, Germany
7 The Mina and Everard Goodman Faculty of Life Sciences, Bar-Ilan University, Ramat-Gan, Israel
8 Department of General Pediatrics, Neonatology and Pediatric Cardiology, University Children's Hospital Duesseldorf, Medical faculty, Heinrich Heine University, Duesseldorf, Germany
9 Rappaport School of Medicine, Technion, Haifa, Israel
10 Pediatric Nephrology Institute, Rambam Health Care Campus, Haifa, Israel
11 Pediatric Epileptology, Bethel Epilepsy Centre, Bielefeld, Germany
12 Department of Radiology, Rambam Health Care Campus, Haifa, Israel
13 Paediatric Neurology and Neuromuscular Disorders, IRCCS Gaslini, Genoa, Italy
14 DINOGMI, University of Genoa, Italy
15 Pediatric Neurology Unit and Epilepsy Service, Meyer Children's Hospital, Rambam Health Care Campus, Haifa, Israel
16 Neurosurgery laboratory, Rambam Health Care Campus, Haifa, Israel
17 Department of Pediatrics, Paracelsus Medical University Salzburg, Salzburg, Austria
18 Metabolic Unit, Rambam Health Care Campus, Haifa, Israel
19 IRCCS Ospedale Policlinico San Martino, Genoa, Italy
20 IRCCS Fondazione Stella Maris, Pisa, Italy

Correspondence to: Prof. Renzo Guerrini (clinical and genetic findings)
Neuroscience Department, Anna Meyer Children's University Hospital, Florence Italy
E-mail: r.guerrini@meyer.it

Correspondence may also be addressed to: Prof. Anna Fassio (functional studies)
Department of Experimental Medicine, University of Genoa, Viale Benedetto XV Genoa, Italy
E-mail: afassio@unige.it

Keywords: developmental and epileptic encephalopathy; Ohtahara syndrome; progressive disorder; autophagy; neuropathy

Introduction

DMXL2 encodes for a vesicular protein, DmX-like protein 2 (DMXL2, also known as rabconnectin-3a), a member of the WD40 repeat (WDR) protein family and harbours 16 WD40 conserved domains and a central Rav1p domain homologous to the yeast v-ATPase regulator Rav1p (Tata *et al.*, 2014). This gene is known to regulate the trafficking and activity of v-ATPase, a multi-subunit proton pump that governs intracellular organelle acidification in all eukaryotic cells and promotes endosomal maturation (Yan *et al.*, 2009; Einhorn *et al.*, 2012; Tuttle *et al.*, 2014). Mammalian DMXL2 is highly expressed in the brain and at synaptic terminals (Nagano *et al.*, 2002; Kawabe *et al.*, 2003; Gobé *et al.*, 2019), where it binds RAB3A interacting proteins as a dimer with DMXL1 (Rabconnectin-3b) but its neurophysiological role remains elusive. *Dmxl2* homozygous knockout mice are embryonic lethal (https://dmdd.org.uk/mutants/Dmxl2) (Tata *et al.*, 2014; Gobé *et al.*, 2019) and heterozygous *Dmxl2* (*Dmxl2*$^{+/-}$) mice show macrocephaly and corpus callosum dysplasia, revealing a role for this gene in brain development (Kannan *et al.*, 2017).

Variants in *DMXL2* have been implicated in human disease through both heterozygous and biallelic models. A heterozygous missense c.7250G>A (p.Arg2417His) mutation has been associated with autosomal dominant non-syndromic hearing loss (Chen *et al.*, 2017). Heterozygous copy number variations (CNVs), either loss or gain, and loss-of-function single nucleotide variants involving *DMXL2*, have been observed in individuals in cohorts with different neurodevelopmental disorders, including autism spectrum disorders (ASD), intellectual disability, and attention-deficit hyperactivity disorder (ADHD), leading to the suggestion that *DMXL2* haploinsufficiency might act as a predisposing factor (Costain *et al.*, 2019). A homozygous in-frame deletion of 15 nucleotides, leading to a five amino acid deletion (p.1942_1946del), has been described in three siblings with growth retardation, moderate intellectual disability, progressive hearing loss and peripheral sensorimotor polyneuropathy-polyendocrine syndrome (PEPNS) (OMIM #616113) (Tata *et al.*, 2014). Finally, a homozygous loss-of-function, likely deleterious truncating c.4349_4350insTTACATGA (p.Glu1450Aspfs*23) variant has been identified in a child with intellectual disability, epilepsy, macrocephaly, dysmorphisms and moderate brain and brainstem atrophy MRI (Maddirevula *et al.*, 2018).

Using whole exome sequencing (WES), we identified homozygous recessive and compound heterozygous mutations of the *DMXL2* gene in six children, belonging to three unrelated families, exhibiting a severe phenotype associated with Ohtahara syndrome, with a persisting burst suppression EEG pattern, profound neurological impairment, sensorineural deafness, mild peripheral polyneuropathy, and dysmorphic features. This disorder exhibited signs of progression, leading to premature death in most patients.

Performing functional studies in patients' fibroblasts, we demonstrated that the DMXL2 protein was absent and that lysosomal function and autophagy were impaired. Analysing *Dmxl2*-silenced mouse hippocampal neurons, we recapitulated defective autophagy and demonstrated impaired neurite development with synaptic loss.

This study demonstrates that biallelic loss-of-function *DMXL2* mutations cause a homogeneously severe phenotype manifested as Ohtahara syndrome with progressive course, which can be categorized within the emerging class of the congenital disorders of autophagy (Ebrahimi-Fakhari *et al.*, 2016; Teinert *et al.*, 2019).

Materials and methods

Study subjects

The three families described here were studied at three different centres (Florence, Italy; Dusseldorf, Germany; and Haifa, Israel). The collaboration leading to this report was initiated through the Gene Matcher platform (https://genematcher.org) (Sobreira *et al.*, 2015). Phenotypic characterization had been obtained in all patients through clinical follow-up, repeated video-EEG recordings, brain MRI and brain auditory evoked potentials. Four patients were also studied with electroneurography (Patients 1-II:1, 1-II:2, 2-II:1 and 2-II:2) and one with a muscle biopsy (Patient 1-II:1).

Parents of all affected siblings gave their consent for the publication of clinical and genetic information according to the Declaration of Helsinki and the study was approved by the respective local Ethic Committees (Family 1: Paediatric Ethic Committee of the Tuscany Region in the context of the DESIRE project, Seventh Framework Programme, grant agreement 602531; Family 2: Ethical Committee of Emek Medical Center; Family 3: Ethic Committee of the Technical University in Munich and of the Heinrich- Heine-University Düsseldorf). Parents of affected siblings of Families 1 and 2 also gave the consent to publish medical photographs of their children.

Whole-exome sequencing and data analysis

Methods used for WES, Sanger sequencing validation and segregation analysis are reported in detail in the Supplementary material.

In silico analyses

We evaluated mutations pathogenicity through *in silico* prediction using the dbNSFP database (v3.3a, Liu *et al.*, 2016) and the scores obtained from Revel (Ioannidis *et al.*, 2016), M-CAP (Jagadeesh *et al.*, 2016) and Eigen (Ionita-Laza *et al.*, 2016), three different tools to rate the pathogenicity of rare variants. Splice variants were evaluated by the dbscSNV (Jian *et al.*, 2017) and SPIDEX (Xiong *et al.*, 2015) tools.

Multiple protein sequence alignment

To assess the conservation of the p.Ala1712Val missense substitution identified in Patients 1-II:1 and 1-II:2, a multiple sequence alignment of DMXL2 orthologous protein sequences was generated by the Jalview software (http://www.jalview.org) with colour-coding for physicochemical properties (Zappo colour scheme).

Muscle biopsy

Muscle biopsy was performed in Patient 1-II:1. The biopsy specimen was taken from the quadriceps muscle and processed according to standard techniques for routine histology and histochemistry (Dubowitz and Sewry, 2007).

Skin biopsy and fibroblasts culture

Skin biopsies were performed in Patients 1-II:1, 2-II:2 and 3-II:5 and fibroblast cell lines were cultured in RPMI medium supplemented with 20% foetal bovine serum (FBS) and 1% penicillin/streptomycin (Thermo Fisher Scientific) at 37°C in a humidified atmosphere with 5% CO_2.

For rescue experiments, 70–80% confluent fibroblasts were transfected with Lipofectamine™ 2000 reagent following the manufacturer's instructions with pCMV6-DMXL2tGFP (Origene #RG230756) or pCMV6-tGFP (Origene #PS100010) and analysed 24 h after transfection.

Reverse transcriptase PCR

Total RNA was extracted from fibroblasts using the RNeasy® Micro Kit (Qiagen) according to the manufacturer's protocol. Complementary DNA (cDNA) was synthesized with the RevertAid First Strand cDNA Synthesis Kit (Thermo Fisher Scientific). RT-PCR was carried out using specific exonic primers encompassing mutated residues. PCR products were analysed by Sanger sequencing.

Primary neuronal cultures and transfection

Primary hippocampal neurons were prepared from embryonic Day 18 brains of C57 Black 6J mice, as previously described (Fassio *et al.*, 2011). Embryonic hippocampi were dissected and incubated in 0.125% trypsin (Gibco) for 25–30 min at 37°C. Dissociated neurons were plated at low density (200 cells/mm^2), onto poly-L-lysine-coated 25 mm glass coverslips. For evaluation of *Dmxl2* silencing, neurons were nucleofected before plating with the 4D-Nucleofector™ System (Lonza) with the high viability protocol for primary mouse neurons and analysed for DMXL2 expression after 7 days. For immunocytochemistry, neurons were transfected at 4 or 14 days *in vitro* (DIV), using Lipofectamine™ 2000 (Thermo Fisher Scientific) and fixed 3 days post-transfection with 4% paraformaldehyde (PFA, Sigma-Aldrich) and 4% sucrose (Applichem) in 1× phosphate-buffered saline (PBS, Sigma Aldrich) at 37°C for 15 min.

Western blotting

Protein lysates from fibroblasts, or primary neurons, were extracted in lysis buffer (50 mM Tris, pH 7.5, 150 mM NaCl, 0.1% SDS, 1% Triton™ X-100, 0.2 mM phenylmethylsulphonyl fluoride, 2 μg/ml pepstatin, and 1 μg/ml leupeptin), separated by SDS-PAGE and assayed by immunoblotting with the following

primary antibodies: anti-DMXL2 (1:500 24415-1-AP; Proteintech; 1:200 ab122552 Abcam), anti-LAMP1 (1:1000; #ab24170, Abcam), anti-EEA1 (1:5000; #610457, BD Bioscience), anti-LC3B (1:1000; #L7543 Sigma-Aldrich), anti-p62 (1:1000, #P0067 Sigma-Aldrich), anti-GAPDH (1:1000; #SC-25778, Santa Cruz Biotechnology), and anti-Ubiquitin (1:200; #sc-8017, Santa Cruz Biotechnology).

Immunocytochemistry and fluorescence microscopy

Cells plated on glass coverslips were washed three times with 1× PBS at 37°C to remove culture medium and fixed by using 4% PFA and 4% sucrose in PBS at 37°C for 15 min. Excess PFA was removed by washing with PBS and cells were permeabilized using 0.1% Triton™ X-100 in PBS for 10 min. Non-specific epitopes were saturated with 2% FBS (Gibco) in 0.05% Tween-20 PBS. Primary antibodies diluted in PBS/2.5% FBS were applied for 2 h at room temperature or overnight at 4°C. The antibody excess was removed by washing the coverslip three times with PBS and the secondary antibodies added for 45 min at room temperature. Alexa-Fluor® 488 and/or Alexa Fluor® 647 (Thermo Fisher) were incubated for 45 min at room temperature and the excess removed with PBS. Coverslips were mounted by using ProLong™ Diamond antifade reagent (Thermo Fisher), containing 4′,6′-diamidino-2-phenylindole (DAPI) to visualize nuclei.

Capture of confocal images was carried out using a laser scanning confocal microscope (SP8, Leica) with either a 40× or 63× oil-immersion objective. The following antibodies were used: anti-LAMP1 (1:200, #L1418 Sigma-Aldrich), anti-EEA1 (1:500; #610457, BD Bioscience), anti-p62 (1:100, #P0067 Sigma-Aldrich) and anti-LC3B (1:200, 200-401-h57 Rockland) anti-DMXL2 (1:100, HPA039375 Sigma Aldrich). Alexa Fluor™ 568 Phalloidin (1:40, #a12380, Thermo Fisher Scientific) was used for actin labelling. Each image consisted of a stack of images taken through the *z*-plane of the cell.

LysoTracker® and LysoSensor™ experiments

For LysoTracker® Deep Red (Lysotracker L12492, Thermo Fisher Scientific) experiments, fibroblasts were incubated with 200 nM LysoTracker® for 1 h at 37°C and neurons with 50 nM LysoTracker® for 30 min at 37°C. Cells were immediately fixed and analysed within 12 h. Images were taken with confocal microscope, in a single plane, to avoid fading the fluorescent signal. Settings were kept the same for all acquisitions within each experiment.

For pH measurement of intracellular organelles, fibroblasts were incubated with 10 µM LysoSensor™ Yellow/Blue DND-160 (Thermo Fisher) for 3 min at 37°C in culture medium. After three washes in 1× PBS to remove any non-internalized dye, the culture was imaged in HEPES buffer (125 mM KCl, 25 mM NaCl, 25 mM HEPES, pH 7.4) for a maximum of 10 min to avoid cell alkalinization. Cell imaging was performed in epifluorescence (Olympus 1X81) under a 60× oil objective. Three images were collected for each field exciting at 340 ± 10 nm or 380 ± 10 nm and collected with a 400 nm long-pass filter. A pH calibration curve was then collected for each coverslip by using 10 µM monensin in HEPES buffer (pH 7.4 and 7.0) and MES buffer (125 mM KCl, 25 mM NaCl, 25 mM MES pH 6.5, 6.0, 5.5, 5.0, 4.5, 4.0, 3.0). LysoSensor™ Yellow/Blue DND-160 intensity in both channels was calculated after background subtraction and ratio (340/380) were fitted to a linear regression with the GraphPad Prism5 software. Data were best fitted in the range of pH 4.0–6.0. For pH evaluation, measured ratios were converted into absolute pH values by interpolation in the calibration function.

Epidermal growth factor receptor degradation assay

Fibroblasts at 80% of confluence were incubated with 200 ng/ml EGF (PeproTech) for 15 min at 4°C allowing ligand-receptor binding. To synchronize ligand-receptor internalization, ligand-containing medium was replaced by fresh prewarmed medium. Cells were incubated at 37°C allowing ligand-receptor internalization for 0, 0.5, 1 and 4 h in the presence of 10 µg/ml cycloheximide (C4859, Sigma-Aldrich) to inhibit the *de novo* synthesis of epidermal growth factor receptor (EGFR). Total cell lysates were prepared and analysed by western blotting using a rabbit polyclonal anti-EGFR antibody (1/2000; kind gift from Carlo Tacchetti, HSR Milano, Italy) to monitor degradation of the 180 kDa EGFR band.

Dextran degradation assay

To determine the degradation of ectopically transduced dextran, cells were incubated with 20 µg/ml of fluorescein isothiocyanate (FITC) labelled dextran (#46944, MerckMillipore) for 2 h. After washing with RPMI medium, supplemented as described above, cells were incubated with fresh medium for 30 min followed by 5-min incubation with CellMask™ Deep Red Plasma membrane stain (#C10046 Thermo Fisher Scientific) to visualize cells. Cells were fixed with a 4% PFA solution. Single plane images were acquired at confocal microscope by keeping the same settings for all acquisitions.

Electron microscopy

Fibroblasts of Patients 1-II-1 and 3-II:5 were harvested, transferred to 1.5 ml Eppendorf tubes and centrifuged at 1000 rpm for 5 min. The cell pellet was fixed with 1.2% glutaraldehyde in 0.1 M sodium cacodylate buffer, post-fixed in 1% OsO4, 1.5% $K_4Fe(CN)_6$, 0.1 M sodium cacodylate, *en bloc* stained with 10% of uranyl acetate replacement stain (EMS) for 30 min, dehydrated, and flat embedded in epoxy resin (Epon® 812, TAAB). After baking for 48 h, the plastic tube was removed from the Epon® block with a razor blade. The Epon® block containing fibroblast was sectioned using an EM UC6 ultramicrotome (Leica Microsystems). Ultrathin sections (60–70 nm thick) were collected on 200-mesh copper grids (EMS) and observed with a JEM-1011 electron microscope (Jeol) operating at 100 kV using an ORIUS SC1000 CCD camera (Gatan). Images of fibroblasts were acquired at ×2500. Full fibroblasts were then reconstructed and analysed using ImageJ and Adobe Illustrator.

RNA interference constructs

Short hairpin RNA (shRNAs) targeting the coding sequences (GGATGGAGTAGCTGTCATCACTTTACCAC) of human

(NM_015263) and mouse (NM_172771) *DMXL2* mRNAs, and scramble non-effective control shRNA cloned into pRFP-C-RS plasmid were obtained from OriGene Technologies (Cat. No TF519727).

Sholl analysis and synapse quantification

The extent of neurite arborization was evaluated at 7 DIV using Sholl analysis, as previously described (Falace *et al.*, 2010). Concentric circles with radii increasing at regular 10-μm steps were centred to the cell body and the number of intersections was automatically evaluated with the ImageJ/Sholl analysis plug-in. To measure synaptic inputs, neurons were labelled at 17 DIV with anti-synaptophysin antibody (1/500, #101011; Synaptic Systems). To measure excitatory or inhibitory synapses, neurons were labelled with anti-V-GLUT1 (1/500, #135304; Synaptic Systems) and anti-Homer1 (1/200, #160011; Synaptic Systems) or V-GAT (1/500, #131103; Synaptic Systems) and anti-Gephyrin (1/200, #147011; Synaptic Systems) antibodies. Confocal images were acquired with a 60× oil immersion objective. Each image consisted of a stack of images taken through the *z*-plane of the cell. Confocal microscope settings were kept constant for all scans in each experiment. Synaptic boutons immunopositive for synaptophysin and decorating RFP-positive neurites (30 μm starting from the cell body), or RFP-positive cell bodies, were manually counted. The co-localization analysis was performed by evaluating the labelling of the VGLUT1/Homer1 and VGAT/Gephyrin synaptic protein couples. Co-localization puncta with areas of 0.1–2 μm^2 were considered *bona fide* synaptic boutons. Synaptic boutons along RFP-positive neurites (30 μm starting from the cell body) and around RFP-positive cell bodies were automatically counted using ImageJ.

Electrophysiological recordings

Hippocampal neurons were recorded at 17 DIV. Whole patch-clamp recordings in voltage-clamp configuration were made as previously described (Baldelli *et al.*, 2007; Falace *et al.*, 2014). Patch pipettes were obtained from thin borosilicate glass, pulled to a final resistance of 4–5 MΩ, and filled with internal standard solution. Voltage-clamp recordings for spontaneous miniature postsynaptic currents (mPSCs) were performed at −70 mV holding potential and the recordings were acquired at 10 kHz and filtered at 2 kHz. All experiments were performed at room temperature (22–25°C). Data acquisition was performed using Multiclamp 700B and Clampex program (Axon Elektronic). To block the generation and propagation of spontaneous action potentials, tetrodotoxin (TTX; 300 nM) was added to the extracellular solution. For recording miniature excitatory PSCs (mEPSCs), bicuculline methiodide (30 μM) and CGP58845 (5 μM) were added to the Tyrode extracellular solution to block GABAA and GABAB receptors, respectively. The internal solution (K-gluconate) used for the recording of mEPSCs was composed of (in mM) 126 K gluconate, 4 NaCl, 1 $MgSO_4$, 0.02 $CaCl_2$, 0.1 BAPTA, 15 glucose, 5 HEPES, 3 ATP, and 0.1 GTP (pH 7.3 with KOH). For recording miniature inhibitory PSCs (mIPSCs), CNQX (10 μM) and D-AP5 (50 μM) were added to block non-NMDA and NMDA receptors, respectively. The internal solution (K-gluconate) was composed of (in mM) 126 KCl, 4 NaCl, 1 $MgSO_4$, 0.02 $CaCl_2$, 0.1 BAPTA, 15 glucose, 5 HEPES, 3 ATP, and 0.1 GTP (pH 7.3 with KOH). The amplitude and frequency of inhibitory and excitatory miniature events were calculated using a peak detector function set with appropriate threshold amplitudes and areas. The frequency, amplitude and kinetics of miniature PSCs were analysed using the MiniAnalysis program and the Prism software (GraphPad Software, Inc.). All reagents were obtained from Tocris, unless otherwise specified.

Statistical analysis

The normal distribution of experimental data was assessed using the D'Agostino-Pearson normality test. Data with normal distribution were analysed by the unpaired Student's *t*-test; non-normally distributed data were analysed by the Kruskal–Wallis one-way ANOVA on Ranks test, followed by the Dunn's multiple comparison tests using Graphpad 7.0 (Graphpad Software Inc., La Jolla, CA). Significance level was preset to $P < 0.05$. Data are expressed throughout as means ± standard error of the mean (SEM) for number of experimental sessions or number of cells analysed (*n*).

Data availability

The authors confirm that the data supporting the findings of this study are available within the article and/or its Supplementary material. Raw sequencing data are available from the corresponding authors on request. Primer sequences used for RT-PCR are available upon request.

Results

Clinical findings

Clinical, EEG and MRI findings observed in the six patients are summarized in Table 1 and Fig. 1 and presented in detail in the Supplementary material. Affected siblings were born to a non-consanguineous Italian father and Brazilian mother in Family 1, to first degree Israeli Arab cousins in Family 2, and to first degree Turkish cousins in Family 3. In brief, all patients exhibited a remarkably similar phenotype that, in addition to the Ohtahara syndrome starting in the first days of life, included profound developmental delay, muscular hypotonia, quadriparesis, sensorineural hearing loss and dysmorphic features (Supplementary Fig. 1). All four affected children in Families 1 and 2 also exhibited mild peripheral polyneuropathy, while no nerve conduction studies were carried out in Family 3. Dosage of co-enzyme Q in the biopsied muscle tissue of Patient 1-II:1 revealed no abnormality. However, microscopy demonstrated abundant lipid droplets, representing storage material, in the sarcoplasm of muscle cells (Supplementary Fig. 2).

In all patients, the suppression burst EEG pattern was continuous, rendering it difficult to differentiate wakefulness and sleep, and remained unchanged throughout follow-up (Fig. 1). Associated seizures were mainly tonic

or, less frequently, myoclonic. Occasional focal seizures occurred in most children. Early brain MRI investigations in the first months of life revealed thin corpus callosum with brain hypomyelination in all. A simplified gyral pattern, without cortical thickening, was observed in Patients 3-II:4 and 3-II:5. The cortical abnormality was limited to the frontal lobes in Patient 3-II:4 and diffuse with frontal predominance in Patient 3-II:5. In the three patients undergoing repeat MRI scans 9 to 21 months after the first scan (Patients 1-II:1, 2-II:2 and 3-II:4), progressive moderate grey and white matter shrinkage with leukoencephalopathy became apparent (Table 1 and Fig. 1).

Five patients died within the first 9 years of life due to respiratory or systemic complications of the severe neurological condition and none achieved developmental, communicative or motor skill following birth (Table 1). One patient was still alive at age 15 months. Age range of the six patients' parents at the time of writing ranged from 39 to 51 years. None of them had ever exhibited neurological symptoms or hearing impairment.

Identification of *DMXL2* mutations by whole exome sequencing

Using WES, we identified biallelic *DMXL2* mutations in all three sibling pairs with Ohtahara syndrome (Fig. 2A and B). Siblings in Family 1 were compound heterozygous for the c.5135C>T (p.Ala1712Val) missense substitution and the c.4478C>G (p.Ser1493*) nonsense substitution; siblings in Family 2 were homozygous for the c.4478C>A (p.Ser1493*) nonsense substitution and in Family 3 were homozygous for the c.7518-1G>A substitution, predicted to alter mRNA splicing by the dbscSNV and SPIDEX tools (Supplementary Table 1) and result in the loss of the canonical splice acceptor site of exon 31.

None of the variants identified in *DMXL2* were reported in the gnomAD database (Supplementary Table 1). The p.Ala1712Val missense substitution affects a highly conserved amino acid residue (Fig. 2C) and is predicted to be damaging by *in silico* tools (Supplementary Table 1). In each family, segregation analysis showed both parents to be heterozygous carriers for the variants (Supplementary Fig. 3).

Effect of *DMXL2* mutations on mRNA and protein expression

Immunoblot analysis performed on skin fibroblasts taken from Patients 1-II:1, 2-II:2 and 3-II:5 revealed almost absent DMXL2 protein (Fig. 2A). RT-PCR analysis on patients' fibroblast RNA revealed that *DMXL2* mRNA was expressed only in Patient 1-II:1; however, the transcript of the allele harbouring the c.4478C>G nonsense mutation was degraded (Supplementary Fig. 4A and B). In Patient 2-II:2, harbouring a homozygous nonsense mutation (c.4478C>A; p.Ser1493*), *DMXL2* mRNA was absent (Supplementary Fig. 4A). Finally, the splice variant c.7518-1G>A, identified in homozygosity in Patient 3-II:5, resulted in the skipping of exon 31, leading to a frameshift and premature termination of protein translation (p.Trp2508Argfs*4; Supplementary Fig. 4C). No low molecular weight immunoreactive protein bands were detected in fibroblast lysates (Supplementary Fig. 4D), suggesting an unstable and degraded mRNA or protein.

DMXL2 mutations result in lysosomal and autophagy abnormalities

As loss of DMXL2 has been associated with impaired v-ATPase activity in multiple experimental models (Yan *et al.*, 2009; Einhorn *et al.*, 2012; Tuttle *et al.*, 2014; Merkulova *et al.*, 2015), we analysed intracellular acidic compartments in Patient 1-II:1 by staining fibroblasts with the acidotropic dye LysoTracker®. The patient's cells showed an increased LysoTracker® signal (Fig. 3A); a phenotype that was confirmed in fibroblasts from Patients 2-II:2 and 3-II:5 (Supplementary Fig. 5). The LysoTracker® signal was reversed by re-expression of the human DMXL2 protein in the patient's fibroblasts (Supplementary Fig. 6). An increased LysoTracker® signal can be contributed to by an expansion of endolysosomal organelles and/or decreased intravesicular pH. Endosomal marker EEA1 and lysosomal marker LAMP1 were significantly decreased, as observed by single cell immunocytochemistry and western blotting (Fig. 3B–D). Measuring intracellular organelle pH with the ratiometric dye LysoSensor™ DND 160, we found that on average the pH within acidic organelles was lower in fibroblasts (Supplementary Fig. 7). To analyse lysosomal function, we evaluated EGF-induced degradation of EGF receptors and degradation of ectopically introduced dextran. Both assays revealed a slowdown of the lysosomal degradative capacity comparing Patient 1-II:1 with control fibroblasts (Fig. 3E and F). These data suggest that DMXL2 loss results in an acidic shift in the intra-organelle pH with impairment of endolysosomal structures and function.

Lysosomal function is intimately linked to autophagy, as lysosomes are targeted by autophagosomes to degrade engulfed materials. We therefore investigated the autophagy process by measuring total LC3 levels and LC3II/LC3I ratio in fibroblasts. Cells from Patient 1-II:1 displayed decreased total LC3 signal, as well as decreased ratio of active membrane-bound LC3II versus cytosolic LC3I (Fig. 4A and C). The patient's fibroblasts also exhibited both increased p62 signal (Fig. 4B and C) and upregulation of high molecular weight polyubiquitinated proteins (Fig. 4D). The observed phenotype suggests defective autophagy with accumulation of autophagy receptors and substrates. Impaired lysosomal/autophagic function was further confirmed by ultrastructural analysis, showing vacuolization and a significant accumulation of atypical fusion-like structures (Supplementary Fig. 8).

Table 1 Genetic and clinical characteristics of six patients with biallelic *DMXL2* mutations identified in this study

	Family 1		Family 2		Family 3	
Age at last FU	4 y (deceased)	5 y 10 m (deceased)	1 y 7 m (deceased)	9 y (deceased)	3 y (deceased)	10 m
Gender	M	F	M	F	M	F
Birth features						
Apgar	10, 10	10, 10	9, 9	2, 4	6, 7	4, 6
Weight/ height	3040 g/49 cm	2700 g/49 cm	3200 g/n.d.	3080 g/n.d.	2980 g/49 cm	1890 g/43.5 cm
Head size	34 cm (20th %ile)	34 cm (29th %ile)	38 cm (90th %ile)	39 cm (99th %ile = +2.3 SD)	35 cm (77th %ile)	30 cm (78th %ile)
Consanguinity	No	No	Yes	Yes	Yes	Yes
Seizures						
Onset	At birth	At birth	At birth	At birth	At birth	At birth
Type	Focal clonic/tonic/spasms	Focal clonic/tonic/spasms	Myoclonic/spasms	Myoclonic/spasms	Myoclonic/tonic	Tonic/spasms
FU	Unchanged	Unchanged	Unchanged	Unchanged	Unchanged	Unchanged
EEG	Burst suppression and multifocal	Burst suppression and multifocal	Burst suppression and multifocal	Burst suppression and multifocal	Burst suppression and multifocal	Burst suppression and multifocal
AEDs						
Used	Multiple including ACTH	Multiple including ACTH	PB	Multiple	Multiple	Multiple
Response	Drug resistant	Drug resistant	Drug resistant	Drug resistant	Drug resistant	Drug resistant
Dysmorphic features						
Face-head	Mild downslanting of palpebral fissures, epicanthal folds, short forehead, saddle nose, myopathic facies, high arched palate	Mild downslanting of palpebral fissures, epicanthal folds, short forehead, saddle nose, myopathic facies, high arched palate	Slight downslanting of palpebral fissures, epicanthal folds, short forehead, saddle nose, myopathic facies, high arched palate, dolichocephaly	Slight downslanting of palpebral fissures, epicanthal folds, short forehead, saddle nose, myopathic facies, high arched palate, dolichocephaly	Slight downslanting of palpebral fissures, epicanthal folds	Slight downslanting of palpebral fissures, epicanthal folds
Additional	None	Non-pitting oedema of limbs, pubic hair growth with normal endocrine profile	Non-pitting oedema of limbs	Non-pitting oedema of limbs, obesity, hirsutism of the four limbs	None	Pubic hair growth with normal endocrine profile
Hearing	Impaired conduction on brainstem auditory evoked responses	Sensorineural hearing loss	Sensorineural hearing loss	Severe sensorineural hearing impairment, prolonged central conduction times along the auditory pathway.	Sensorineural hearing loss	Sensorineural hearing loss
PPN	+ (mild)	+ (mild)	+	+	n.d.	n.d.
Neurological examination	Severe hypotonia, quadriplegia, no spontaneous movements, no milestones acquired, profound ID, no eye tracking	Severe hypotonia, quadriplegia, no spontaneous movements, no milestones acquired, profound ID, no eye tracking	Early severe hypotonia, no spontaneous movements, no milestones acquired, later hypertonia, profound ID, no eye tracking	Early severe hypotonia, no spontaneous movements, no milestones acquired, later hypertonia, profound ID, no eye tracking, PEG tube	Early severe hypotonia, no spontaneous movements, no milestones acquired, later hypertonia, profound ID, no eye tracking, PEG tube	Early severe hypotonia, no spontaneous movements, no milestones acquired, later hypertonia, profound ID, no eye tracking, PEG tube
Head size	7 mo: 42 cm (4th %ile); 4 y: 45 cm (<1st %ile = −3.6 SD)	7 mo: 41 cm (6th %ile); 4 y: 44 cm (<1st %ile = −3.6 SD)	1 y: 47.3 cm (69th %ile)	1 y: 49 cm (>99th %ile = +3 SD)	10 mo: 50 cm (>99th %ile = +3.1 SD)	3 mo: 41 cm (78th %ile)
MRI (age and features)	At birth: Thin corpus callosum; at 16 months: delayed myelination/leukoencephalopathy, thin corpus callosum mild atrophy	At birth: Thin corpus callosum	5 mo: Thin corpus callosum, hypomyelination, mild cortical atrophy, dilated ventricles	3 mo: Thin corpus callosum; at 2 y: hypomyelination/leukoencephalopathy, thin corpus callosum cortical atrophy/dilated ventricles	1 mo: Thin corpus callosum; simplified gyral pattern, with normal cortical thickness, in the frontal lobes; at 10 m0: hypomyelination / leukoencephalopathy	1 mo: Thin corpus callosum; diffusely, anterior predominant, simplified gyral pattern with normal cortical thickness
Mutation	(i) chr15:g.51780233G>A NM_015263.3: c.5135C>T p.Ala1712Val (ii) chr15:g.51790943G>C NM_015263.3: c.4478C>G p.Ser1493*	(i) chr15:g.51780233G>A NM_015263.3: c.5135C>T p.Ala1712Val (ii) chr15:g.51790943G>C NM_015263.3: c.4478C>G p.Ser1493*	(i) chr15:g.51790943G>T NM_015263.3: c.4478C>A p.Ser1493*	(i) chr15:g.51790943G>T NM_015263.3: c.4478C>A p.Ser1493*	(i) chr15:g.51757849C>T NM_015263.3: c.7518-1G>A p.Trp2507Argfs*4	(i) chr15:g.51757849C>T NM_015263.3: c.7518-1G>A p.Trp2507Argfs*4
Mutation status	Compound heterozygous	Compound heterozygous	Homozygous	Homozygous	Homozygous	Homozygous

ACTH = adrenocorticotropic hormone; AED = antiepileptic drug; FU = follow-up; mo = months; n.d. = not determined; PB = phenobarbital; PPN = peripheral polyneuropathy; y = years.

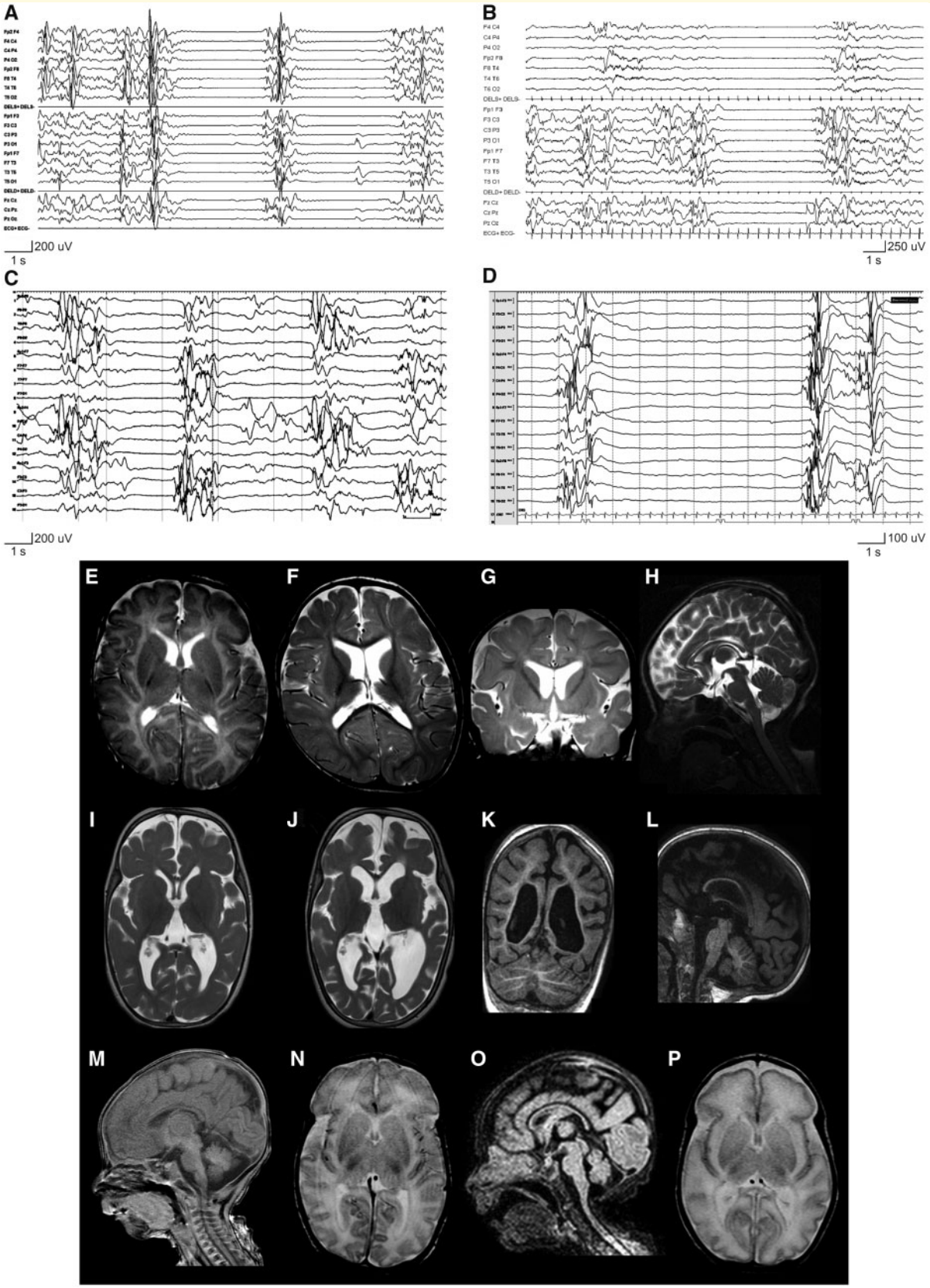

Figure 1 EEG recordings and brain MRI. (**A**–**D**) EEG recordings in Patients 1-II:1 (**A**, at 4 years), 1-II:2 (**B**, at 3 years), 3-II:4 (**C**, at 3 months) and 3-II:5 (**D**, at 4 months). All four patients show a similar suppression burst EEG pattern. (**E**–**P**) Brain MRI of Patients 1-II:1 (**E**–**H**), 2-II:2 (**I**–**L**), 3-II:4 (**M** and **N**) and 3-II:5 (**O** and **P**). Note the progressive brain atrophy with ventricular dilatation in Patients 1-II:1 (**E** and **F** are taken at 2 months and 16 months, respectively) and 2-II:2 (**I** and **J** are taken at 3 months and 2 years, respectively). There is also diffuse

(continued)

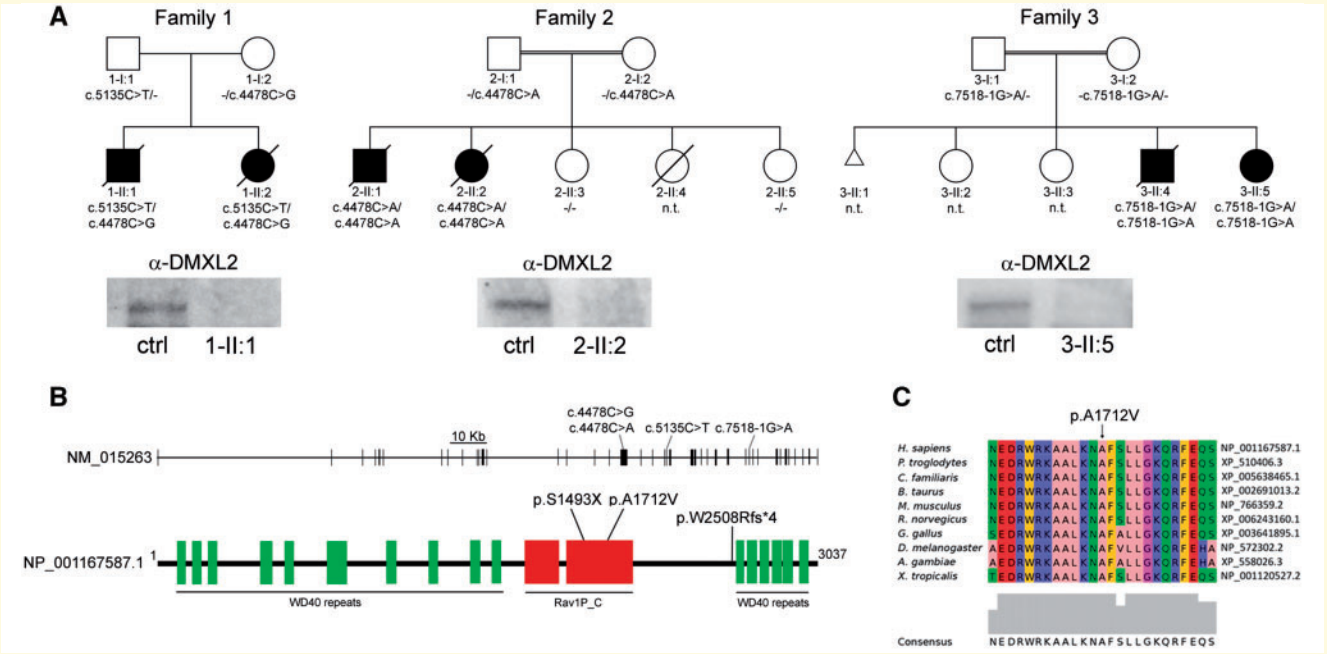

Figure 2 Identification of biallelic mutations in *DMXL2*. (**A**) Pedigrees of Families 1, 2 and 3, with indication of the *DMXL2* alleles below each tested individual. DMXL2 protein expression in the indicated proband and relative control fibroblasts is shown below each family pedigree. (**B**) Schematics showing the organization of *DMXL2* gene and conserved domains of DMXL2 protein with localization of the identified mutations. (**C**) Multiple sequence alignment between human DMXL2 and orthologous sequences encompassing the alanine 1712 (A1712) residue. Residues were coloured according to their physicochemical properties (Zappo colour scheme).

DMXL2 loss impacts on neuronal autophagy, development and synaptic contacts

In view of the prominent neurological impairment of these six patients, harbouring severe *DMXL2* loss-of-function mutations, we modelled neuronal *DMXL2* loss by silencing its expression in primary neuronal cultures. We transfected *Dmxl2* shRNA, tested for its efficacy to downregulate DMXL2 neuronal expression (Supplementary Fig. 9), or its scrambled version, in mouse hippocampal neurons.

We first investigated whether the lysosomal/autophagy defects observed in fibroblasts were recapitulated in neurons. In developing neurons at 7 DIV, LysoTracker® staining was significantly increased at cell bodies, upon *Dmxl2* silencing at 4 DIV, with decreased LAMP1 signal (Fig. 5A and B). Silenced neurons also exhibited a significant reduction of LC3 expression at cell soma, accompanied by accumulation of the autophagic receptor p62 (Fig. 5C and D). These data demonstrate that loss of DMXL2 at the single neuron level results in altered lysosomal structures and defective autophagy.

As autophagy-related degradative processes are essential for neuronal function, and have been reported to play pivotal roles in neuronal development and connectivity (Shehata *et al.*, 2012; Tang *et al.*, 2014), we analysed hippocampal neurons at 7 DIV for neurite extension and arborization and found a significant decrease of neurite complexity in *Dmxl2*-silenced cells (Fig. 6A). At later developmental stages neurons establish complex connectivity and form functional networks balancing excitatory and inhibitory inputs. By measuring synaptophysin boutons impinging on *Dmxl2* silenced neurons at 17 DIV (3 days after transfection), we uncovered a significant reduction consistent with an impairment in synaptic connections (Fig. 6B).

Figure 1 Continued
hypomyelination, which is visible as increased signal in the white matter in T_2 (**F**, **G** and **J**) or reduced signal in T_1 (**K**) in both children when re-imaged after age 1 year. Patients 3-II:4 and 3-II:5 where only imaged once when 1 month old; a simplified gyral pattern, without cortical thickening, was observed in both. The cortical abnormality was limited to the frontal lobes in Patient 3-II:4 and was diffuse with frontal predominance in Patient 3-II:5 (**N** and **P**). Patient 3-II:4 had a follow-up MRI at the age of 10 months, in which increased white matter signal had become more conspicuous (not shown). All four patients whose MRIs are presented here exhibit severely hypoplastic/thinned corpus callosum, as visible in sagittal images (**H**, **L**, **M** and **O**).

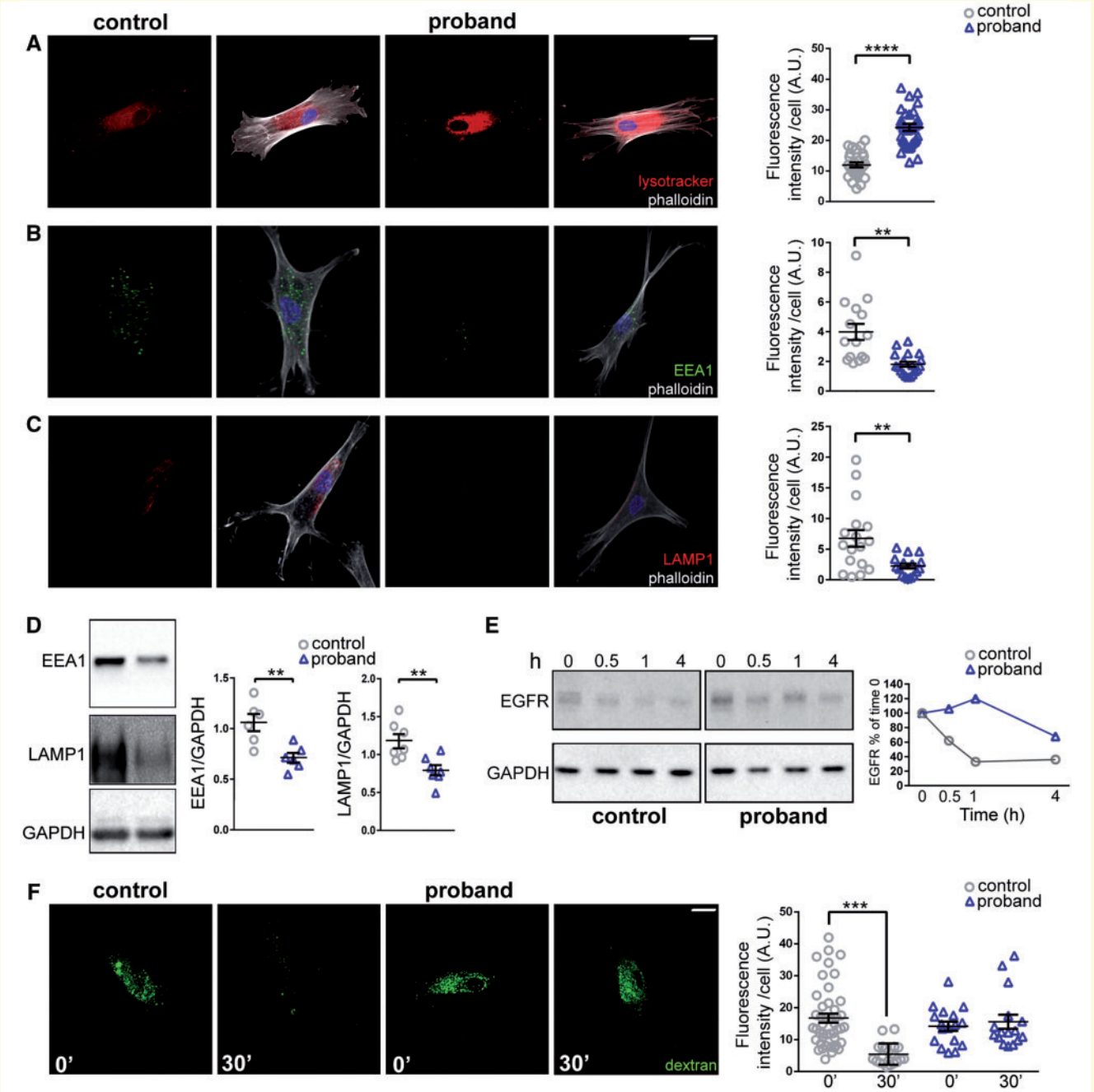

Figure 3 Endolysosomal defects in Patient 1-II:1's cells. (**A**) *Left:* Representative images of fibroblasts from Patient 1-II:1 (proband) and the respective control incubated with LysoTracker® (200 nM, 1 h) and stained with phalloidin. Scale bar = 40 μm. *Right:* LysoTracker® fluorescence intensity (individual data and means ± SEM) was quantified in 27 (control) and 36 (proband) cells. (**B**) *Left:* Representative images of fibroblasts as in **A**, immunolabelled with EEA1 and stained with phalloidin. *Right:* EEA1 fluorescence intensity (individual data and means ± SEM) was quantified in 15 (control) and 19 (patient) cells. (**C**) *Left:* Representative images of fibroblasts as in **A**, immunolabelled with LAMP1 and stained with phalloidin. *Right:* LAMP1 fluorescence intensity (individual data and means ± SEM) was quantified in 17 (control) and 16 (proband) cells. $^{**}P < 0.005$, $^{****}P < 0.001$, unpaired *t*-test with Welch's correction. (**D**) *Left*: Representative western blot of LAMP1, EEA1 and GAPDH obtained from fibroblast lysates (30 μg). *Right:* EEA1 and LAMP1 immunoreactivity were quantified by densitometric analysis and normalized to GAPDH. Data are means ± SEM from six (EEA1) and seven (LAMP1) independent experiments. $^{**}P < 0.005$; Mann- Whitney U-test. (**E**) Western blot of EGFR degradation assay. Control and proband's fibroblasts treated 15 min with 200 ng/ml EGF and washed for the times indicated in the presence of 10 μg/ml cycloheximide. Total cell lysates were analysed with anti-EGFR antibodies to monitor degradation of the EGFR. GAPDH is shown for equal loading. Densitometric quantification, expressed as the percentage of EGFR levels relative to the initial amount, is shown on the *right*. (**F**) *Left*: Representative images of control and proband's fibroblasts treated with FITC-labelled dextran and analysed at the indicated time points. Scale bar = 40 μm. *Right*: Dextran fluorescent intensity (individual data and means ± SEM) was quantified in 20–45 control cells and in 16–17 proband cells. $^{***}P < 0.0001$, Kruskall-Wallis/Dunn's tests. A.U. = arbitrary units of fluorescence intensity.

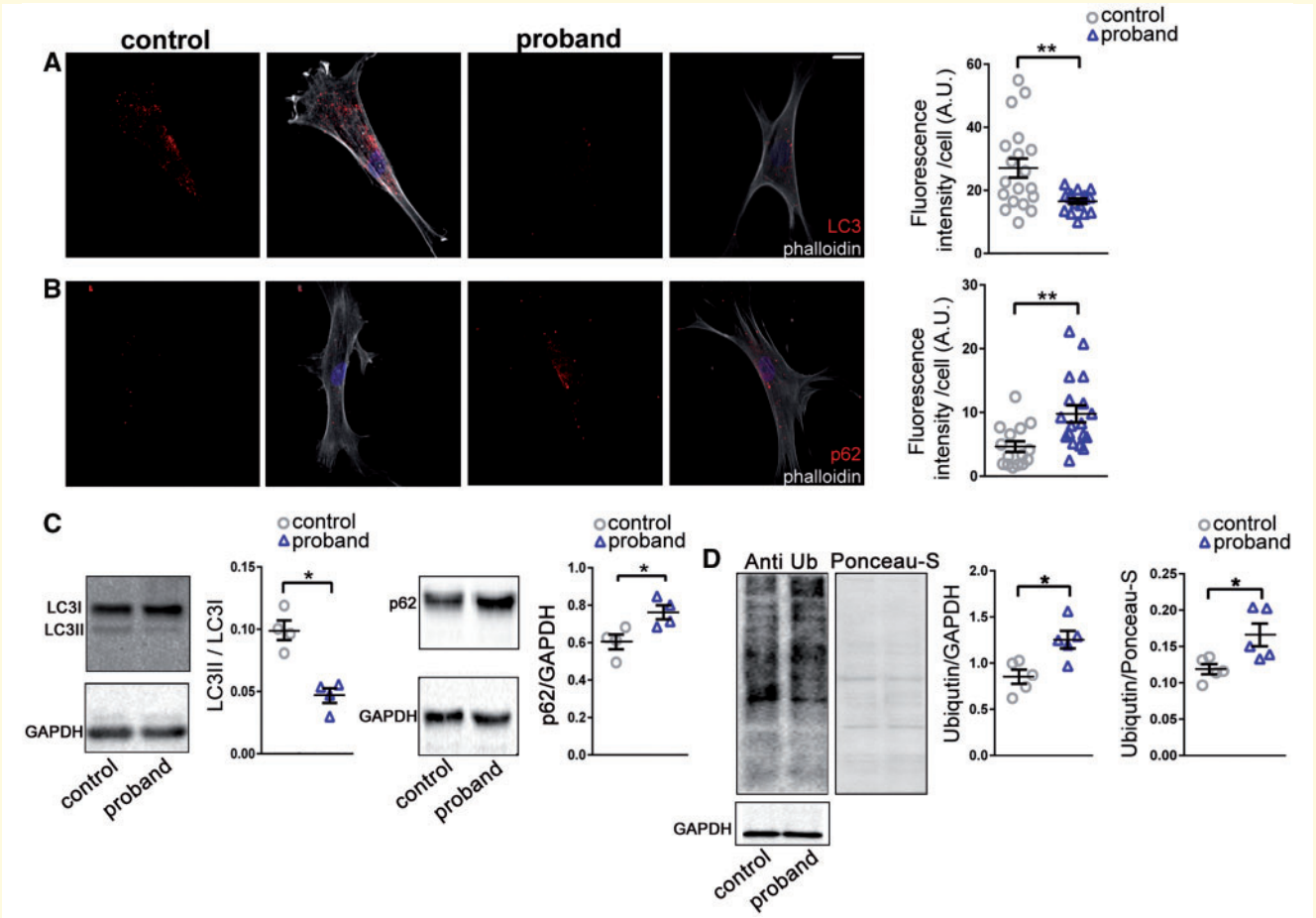

Figure 4 Autophagy defects in Patient 1-II:1's cells. (**A**) *Left:* Representative images of fibroblasts from Patient 1-II:1 (proband) and the respective control immunolabelled with LC3 and stained with phalloidin. Scale bar = 20 μm. *Right:* LC3 fluorescence intensity (individual data and means ± SEM) was quantified in 19 (control) and 16 (proband) cells. $^{**}P < 0.01$; unpaired *t*-test with Welch's correction. (**B**) *Left:* Representative images of fibroblasts as in **A**, immunolabelled with p62 and stained with phalloidin. *Right:* p62 fluorescence intensity (individual data and means ± SEM) was quantified in 15 (control) and 18 (proband) cells. $^{**}P < 0.005$; unpaired *t*-test with Welch's correction. (**C**) Representative western blot of LC3I, LC3II, p62 and GAPDH obtained from fibroblast lysates (30 μg). Immunoreactivity was quantified by densitometric analysis and normalized to LC3I for LC3II, and to GAPDH for p62. Data are means ± SEM from $n = 4$ independent experiments. $^{*}P < 0.05$; Mann-Whitney U-test. (**D**) Representative western blot from fibroblast lysates (30 μg). Ubiquitinated proteins were detected with anti-ubiquitin (Anti-Ub) antibody; GAPDH or Ponceau-S intensity along the lanes were used as loading controls. Ubiquitinated proteins immunoreactivity was quantified by densitometric analysis and normalized to GAPDH or to Ponceau S. Data are means ± SEM from $n = 5$ independent experiments. $^{*}P < 0.05$; Mann-Whitney U-test. A.U. = arbitrary units of fluorescence intensity.

Measuring miniature synaptic currents did not reveal a remarkable difference at this developmental stage, suggesting that the loss involves functionally immature contacts or is prevalent at dendritic, rather than somatic, compartments. Indeed, somatic synaptophysin-positive boutons were unaffected by *Dmxl2* silencing (Supplementary Fig. 10). To identify synapse contacts unambiguously and distinguish between excitatory and inhibitory contacts, we visualized synapses by double immunostaining with the presynaptic and postsynaptic markers VGLUT1/Homer1 or VGAT/Gephyrin, respectively, and confirmed the loss of contacts for *Dmxl2*-silenced neurons, which reached significance for excitatory dendritic connections (Fig. 6C and D). Considering that, under our experimental conditions, *Dmxl2* silenced neurons are mostly surrounded by a naïve neuronal network, these findings suggest a cell autonomous role of DMXL2 in synapse formation.

Overall, results on the neuronal model indicate that, upon DMXL2 loss, neurons undergo neurodevelopmental defects associated with impaired autophagy.

Discussion

Using WES, we identified biallelic *DMXL2* mutations in six children with a consistent Ohtahara syndrome phenotype, belonging to three unrelated families. Affected children also exhibited profound developmental delay, hypotonia,

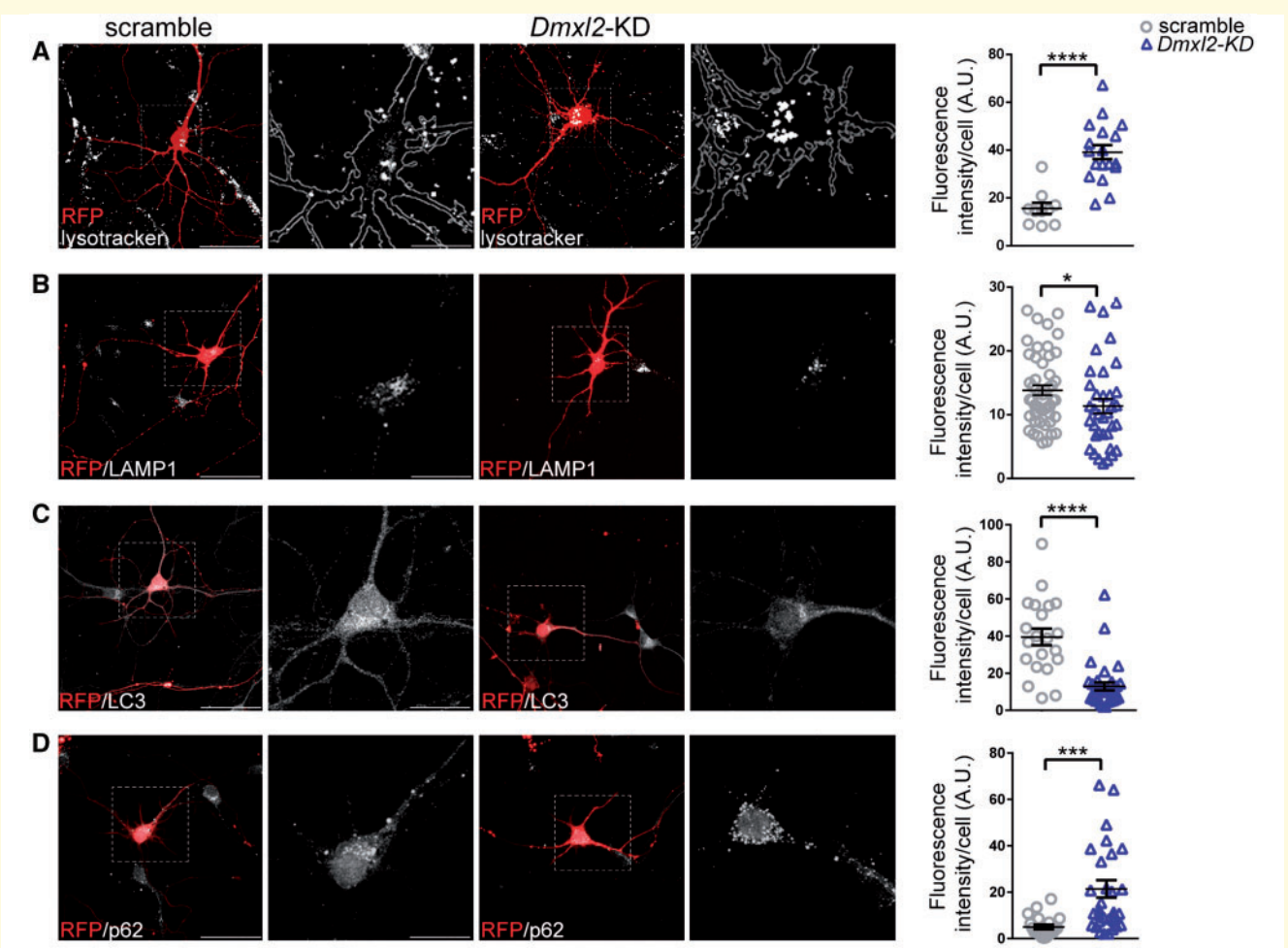

Figure 5 Loss of neuronal *Dmxl2* alters lysosomal and autophagy markers. (**A**) *Left:* Representative images of hippocampal mouse neurons transfected at 4 DIV with control shRNA (scramble) or *Dmxl2* shRNA (*Dmxl2*-KD) harbouring the red fluorescent protein (RFP) reporter and incubated with LysoTracker® (50 nM, 30 min) at 7 DIV. Manual tracing of neuronal surface is shown. Scale bar = 50 μm. White dashed rectangles indicate regions shown at high magnification on the *right*. Scale bar = 125 μm. *Right*: LysoTracker® fluorescence intensity (individual data and means ± SEM) was quantified in 10 (scramble) and 18 (*Dmxl2*-KD) cells from three independent preparations. (**B**–**D**) *Left*: Representative images of hippocampal mouse neurons as in **A** and immunostained for LAMP1 (**B**), LC3 (**C**) or p62 (**D**). Scale bar = 50 μm. White dashed rectangles indicate regions shown at high magnification on the right. Scale bar = 100 μm. *Right*: Respective fluorescence intensity (individual data and means ± SEM) was quantified in 21–37 (scramble) and 27–33 (*Dmxl2*-KD) cells from three independent preparations. A.U. = arbitrary units of fluorescence intensity. $^{*}P < 0.05$, $^{***}P < 0.001$, $^{****}P < 0.0001$ Mann-Whitney unpaired *t*-test.

quadriparesis, dysmorphic features, and sensorineural hearing loss. A mild peripheral polyneuropathy could be demonstrated in the four children explored with nerve conduction studies. The DMXL2 protein was absent in patient-derived skin fibroblasts, supporting a loss-of-function effect for the mutations and consistent with the extreme *DMXL2* phenotype observed in these patients.

Both heterozygous and homozygous *DMXL2* variants had previously been associated with human disease (Tata *et al.*, 2014; Chen *et al.*, 2017; Maddirevula *et al.*, 2018; Costain *et al.*, 2019), although with different levels of substantiation. In a large family with autosomal dominant non-syndromic hearing loss a missense DMXL2 mutation co-segregated with the phenotype (Chen *et al.*, 2017). In addition, heterozygous *DMXL2* loss-of-function mutations and CNVs have been proposed as predisposing factors to ASD, developmental delay/intellectual disability, and ADHD (Costain *et al.*, 2019), though with variable expressivity and incomplete age-related penetrance. A biallelic in-frame deletion was identified in children with a peripheral sensorimotor polyneuropathy-polyendocrine (PEPN) syndrome, dystonia and moderate intellectual disability (Tata *et al.*, 2014). A biallelic loss-of-function frameshift insertion (c.4349_4350insTTACATGA; p.Glu1450Aspfs ∗23, to be referred to as p.Lys1451Tyrfs∗14 using the Human NM_015263 *DMXL2* accession number) was identified in a 3-year-old boy with a phenotype closer to that observed in our patients, including severe intellectual disability, early onset focal seizures, macrocephaly, facial dysmorphisms and moderate brain and brainstem atrophy at MRI (Maddirevula *et al.*, 2018). Overall, the above evidence

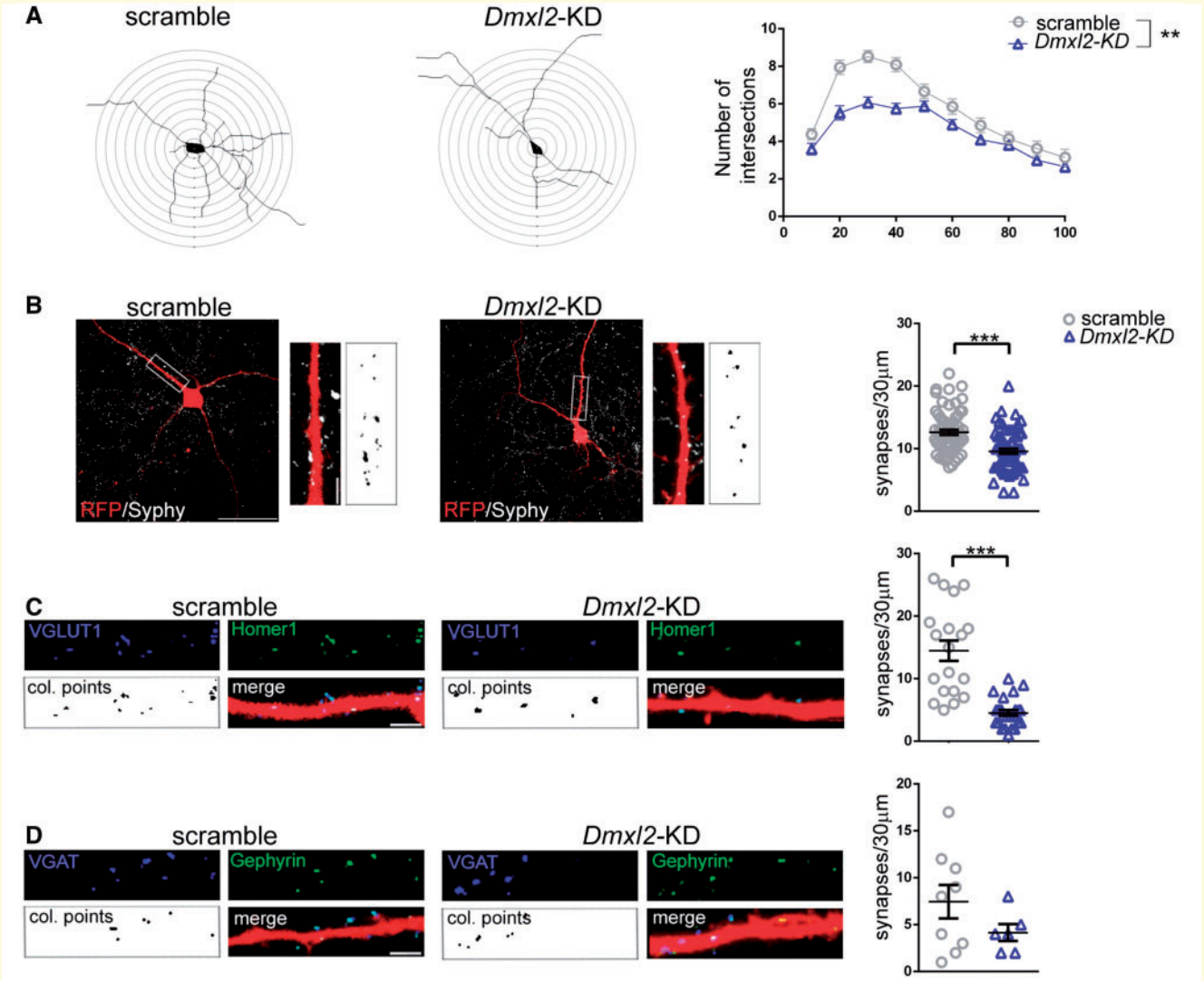

Figure 6 Loss of *Dmxl2* affects neurite arborization and synaptic contacts. (**A**) *Left*: Representative neuronal reconstructions with concentric circles of radii increasing in 10-µm increments for Sholl analysis. *Right*: Sholl analysis of neurite arborization as a function of distance from the soma. Data are means ± SEM of 21 (scramble) and 32 (*Dmxl2*-KD) neurons per experimental condition from three independent experiments. (**B**) *Left*: Representative images of mouse hippocampal neurons transfected at 14 DIV with control shRNA (scramble) or *Dmxl2* shRNA (*Dmxl2*-KD) harbouring the red fluorescent protein (RFP) reporter and immunostained for synaptophysin (Syphy) at 17 DIV. Scale bar = 50 µm. White rectangles indicate the regions shown at higher magnification on the *right*. The black and white panels show positive puncta along branches of transfected neurons. Scale bar = 5 µm. *Right*: Quantitative analysis of synaptic puncta counted on 30-µm branches starting from the cell body. Data are means ± SEM of 46–52 neurons per experimental condition, from three independent preparations. (**C** and **D**) *Left*: High magnifications of proximal dendrites from hippocampal neurons treated as in **B**. Excitatory and inhibitory synaptic boutons were identified by double immunostaining with VGLUT1/Homer 1 and VGAT/Gephyrin, respectively. The merge panels show positive puncta along transfected branches. The co-localization panels (col. points) highlight the double-positive puncta (black) along transfected branches, corresponding to *bona fide* synapses. Scale bar = 6µm. *Right*: Quantitative analysis of synaptic puncta counted on 30-µm branches starting from the cell body. Data are means ± SEM of 10–26 neurons per experimental condition, from two independent preparations. $^{**}P < 0.01$, $^{***}P < 0.001$, unpaired *t*-test with Welch's correction.

convincingly indicates that *DMXL2* variants cause disease but leaves uncertainty whether heterozygous variants also do. The observation that all heterozygous mutation carriers in the five families exhibiting recessive inheritance so far described, including the three participating in this study, appeared to be healthy, casts further doubt on the role of heterozygous variants.

Differences in severity between the milder PEPN phenotype and the profound encephalopathy we observed point to some initial genotype-phenotype correlations. PENP derives from a biallelic in-frame deletion with 30% *DMXL2* residual transcript (Tata *et al.*, 2014), while in our patients, loss-of-function mutations, with no residual protein, had a more severe impact on the developing nervous system.

The severe neurological impairment and persistent suppression burst EEG in *DMXL2* encephalopathy consistently reflect severely impaired neural connections. In the immature brain, before 30–32 weeks of gestation, a suppression burst EEG pattern is physiological; however, in various developmental disorders it persists, reflecting disruption of brain connectivity (Aicardi and Ohtahara, 2005). Electrophysiological studies in cats have demonstrated that responsiveness of cortical and thalamic neurons to orthodromic volleys is dramatically reduced during the suppression periods, a finding that testifies for a severe disruption in brain circuits involved in EEG generation (Steriade *et al.*, 1994). The severe clinical phenotype observed in all six children we describe here, associated with hypomyelination, corpus callosum dysgenesis and progressive brain atrophy, is in keeping with a developmental brain disorder that begins in the prenatal brain, prevents neural connections from reaching the expected stages at birth and follows a progressive course, leading to early lethality.

Dmxl2 homozygous knockout mice are embryonic lethal (https://dmdd.org.uk/mutants/Dmxl2) (Tata *et al.*, 2014; Gobè *et al.*, 2019) and heterozygous *Dmxl2* (*Dmxl2*$^{+/-}$) mice show macrocephaly and corpus callosum dysplasia, confirming a role for this gene in brain development (Kannan *et al.*, 2017). By investigating the consequences of *Dmxl2* deficiency on the maturation of GnRH hypothalamic neurons in the mouse brain, Tata *et al.* (2017) observed a reduced transition from the immature to the mature stage.

We demonstrated that patient-derived skin fibroblasts exhibited perturbation of endolysosomal homeostasis associated with impaired autophagy, an evolutionarily conserved lysosomal degradation process indispensable for cell homeostasis. Studying *Dmxl2*-silenced neurons, we recapitulated the defective lysosomal and autophagy phenotype observed in patients' fibroblasts and highlighted impaired neurite development and synapse formation.

The association of profound neurological impairments, epilepsy, hearing loss and polyneuropathy at birth, observed in our patients, indicates an overall dysfunction of multiple neuronal populations, most likely driven by impaired autophagy. These findings are in line with emerging evidence indicating a role for v-ATPase regulation and autophagy in shaping neuronal connectivity and function and their involvement in developmental encephalopathies (Vijayan *et al.*, 2017; Fassio *et al.*, 2018; Gstrein *et al.*, 2018, Lieberman *et al.*, 2019; Marsh *et al.*, 2019; Hirose *et al.*, 2019). Decreased endolysosomal markers and defective lysosomal degradation, together with cytoplasmic vacuolization and atypical autophagolysosome-like structures observed on electron microscopy in patients' fibroblasts, suggest that impaired autophagy is secondary to impaired lysosomal function. Lipidic infiltrates demonstrated in the muscle of Patient 1-II:1 are also in keeping with impaired lysosomal function.

In recent years, a number of genetic defects in the autophagy pathway have been described, leading to prominent involvement of the CNS, peripheral nerve and skeletal muscle (Ebrahimi-Fakhari *et al.*, 2014, 2016). One such condition bears considerable similarities with the *DMXL2* encephalopathy we describe, including a severe, life-limiting course, and results from biallelic mutations of *EPG5* (Vici syndrome: OMIM #242840), whose function is mainly exerted on autophagosome-lysosome fusion (Cullup *et al.*, 2013; Byrne *et al.*, 2016; Wang *et al.*, 2016). Vici syndrome is considered a paradigm of neurodevelopmental conditions characterized by primary autophagic defects, manifested by profound early hypotonia, with subsequent failure to achieve any developmental milestone, associated with corpus callosum agenesis, microcephaly, and failure to thrive, with variable multi-organ involvement. Epilepsy, present in ~60% of patients, has variable, yet early, age at onset and expression, including Ohtahara syndrome (Byrne *et al.*, 2016) and other severe forms. Sensorineural hearing impairment, cataracts, optic atrophy, hypopigmentation, cardiomyopathy and skeletal myopathy are also present in most patients.

DMXL2 encephalopathy does not feature multi-organ involvement. However, like Vici syndrome, it is associated with central and peripheral nervous system involvement in a context of profound neurodevelopmental impairment, severely reducing life expectancy. The most prominent feature of *DMXL2* encephalopathy is the relentless epileptic activity, manifested as Ohtahara syndrome from birth onward, with no age-dependent modification. At the neuronal circuitry level, the neurite elongation defect and reduced synaptic contacts, associated with DMXL2 loss, could lead to excitation/inhibition imbalance and recurrent seizures. Although further studies are needed to decipher the role of DMXL2 in synapse formation and function, our data indicate a crucial role of this protein in neuronal autophagy, as suggested for other members of the WDR protein family (Saitsu *et al.*, 2013; Kannan *et al.*, 2017). A decrease in the autophagy marker LC3II and accumulation of protein substrates in patients' cells and in the neuronal model of DMXL2 loss, suggest that defective autophagy underlies both the neurodevelopmental defects and the observed clinical phenotype.

We establish DMXL2 encephalopathy as an additional neurodevelopmental condition with early clinical expression and progressive course related to lysosomal and autophagy defects (Ebrahimi-Fakhari *et al.*, 2014, 2016). Our findings further point to autophagy as a key and indispensable cellular process for CNS development.

Acknowledgements

We thank Claudia Bianchini (Children's Hospital A. Meyer) for her help in the NGS data analysis of Family 1. We thank Alona Zilberberg and Sol Efroni (Bar-Ilan University) for their help in culturing fibroblasts of

Patient 2-II:2, Morad Hayat and Chen Gafni (Emek Medical Center) for helpful discussions regarding the molecular data of Family 2. We thank Dirk Klee (Heinrich-Heine University Düsseldorf) for the evaluation of MRI images of Patients 3-II:4 and 3-II:5, Christoph Damaschke (Sana- Klinikum Remscheid) for helpful discussions regarding the clinical phenotypes of Patients 3- II:4 and 3-II:5. We thank Drs Silvia Casagrande and Sara Pepe for their assistance in culturing fibroblasts and hippocampal primary neurons and live imaging experiments.

Funding

This study was supported by grants from the European Commission (Seventh Framework Programme FP7 under the project DESIRE grant agreement n° 602531), the German Research Foundation/Deutsche Forschungsgemeinschaft (DI 1731/2-1 to F.D.), and the "Elterninitiative Kinderkrebsklinik e.V." (Düsseldorf; #701900167).

Competing interests

The authors declare no competing interests.

Supplementary material

Supplementary material is available at *Brain* online.

References

Aicardi J, Ohtahara S. Severe neonatal epilepsies with suppression-burst pattern. In: Roger J, Bureau M, Dravet C, Genton P, Tassinari CA, Wolf P, editors. Epileptic syndromes in infancy, childhood and adolescence. Montrouge: John Libbey Eurotext; 2005. p. 39–52.

Baldelli P, Fassio A, Valtorta F, Benfenati F. Lack of synapsin I reduces the readily releasable pool of synaptic vesicles at central inhibitory synapses. J Neurosci 2007; 27: 13520–31.

Byrne S, Jansen L, U-King-Im J-M, Siddiqui A, Lidov HGW, Bodi I, et al. EPG5-related Vici syndrome: a paradigm of neurodevelopmental disorders with defective autophagy. Brain 2016; 139: 765–81.

Chen DY, Liu XF, Lin XJ, Zhang D, Chai YC, Yu DH, et al. A dominant variant in DMXL2 is linked to nonsyndromic hearing loss. Genet Med 2017; 19: 553–8.

Costain G, Walker S, Argiropoulos B, Baribeau DA, Bassett AS, Boot E, et al. Rare copy number variations affecting the synaptic gene DMXL2 in neurodevelopmental disorders. J Neurodev Disord 2019; 11: 3.

Cullup T, Kho AL, Dionisi-Vici C, Brandmeier B, Smith F, Urry Z, et al. Recessive mutations in EPG5 cause Vici syndrome, a multisystem disorder with defective autophagy. Nat Genet 2013; 45: 83–7.

Dubowitz V, Sewry CA. The procedure of muscle biopsy. In: Muscle biopsy. Saunders Elsevier; 2007. p. 3–20.

Ebrahimi-Fakhari D, Saffari A, Wahlster L, Lu J, Byrne S, Hoffmann GF, et al. Congenital disorders of autophagy: an emerging novel class of inborn errors of neuro-metabolism. Brain 2016; 139: 317–37.

Ebrahimi-Fakhari D, Wahlster L, Hoffmann GF, Kölker S. Emerging role of autophagy in pediatric neurodegenerative and neurometabolic diseases. Pediatr Res 2014; 75: 217–26.

Einhorn Z, Trapani JG, Liu Q, Nicolson T. Rabconnectin3α promotes stable activity of the H+ pump on synaptic vesicles in hair cells. J Neurosci 2012; 32: 11144–56.

Falace A, Buhler E, Fadda M, Watrin F, Lippiello P, Pallesi-Pocachard E, et al. TBC1D24 regulates neuronal migration and maturation through modulation of the ARF6-dependent pathway. Proc Natl Acad Sci U S A 2014; 111: 2337–42.

Falace A, Filipello F, La Padula V, Vanni N, Madia F, De Pietri Tonelli D, et al. TBC1D24, an ARF6-interacting protein, is mutated in familial infantile myoclonic epilepsy. Am J Hum Genet 2010; 87: 365–70.

Fassio A, Esposito A, Kato M, Saitsu H, Mei D, Marini C et al. De novo mutations of the ATP6V1A gene cause developmental encephalopathy with epilepsy. Brain 2018; 141: 1703–18.

Fassio A, Patry L, Congia S, Onofri F, Piton A, Gauthier J, et al. SYN1 loss-of-function mutations in autism and partial epilepsy cause impaired synaptic function. Hum Mol Genet 2011; 20: 2297–307.

Gobé C, Elzaiat M, Meunier N, André M, Sellem E, Congar P, et al. Dual role of DMXL2 in olfactory information transmission and the first wave of spermatogenesis. PLOS Genet 2019; 15: e1007909.

Gstrein T, Edwards A, Přistoupilová A, Leca I, Breuss M, Pilat-Carotta S, et al. Mutations in Vps15 perturb neuronal migration in mice and are associated with neurodevelopmental disease in humans. Nat Neurosci 2018; 21: 207–17.

Hirose T, Cabrera-Socorro A, Chitayat D, Lemonnier T, Féraud O, Cifuentes-Diaz C et al. ATP6AP2 variant impairs CNS development and neuronal survival to cause fulminant neurodegeneration. J Clin Invest 2019; 130: 2145–62.

Ioannidis NM, Rothstein JH, Pejaver V, Middha S, McDonnell SK, Baheti S, et al. REVEL: an ensemble method for predicting the pathogenicity of rare missense variants. Am J Hum Genet 2016; 99: 877–85.

Ionita-Laza I, McCallum K, Xu B, Buxbaum JD. A spectral approach integrating functional genomic annotations for coding and noncoding variants. Nat Genet 2016; 48: 214–20.

Jagadeesh KA, Wenger AM, Berger MJ, Guturu H, Stenson PD, Cooper DN, et al. M-CAP eliminates a majority of variants of uncertain significance in clinical exomes at high sensitivity. Nat Genet 2016; 48: 1581–6.

Jian X, Liu X. In silico prediction of deleteriousness for nonsynonymous and splice-altering single nucleotide variants in the human genome. Methods Mol Biol 2017; 1498: 191–7.

Kannan M, Bayam E, Wagner C, Rinaldi B, Kretz PF, Tilly P, et al. WD40-repeat 47, a microtubule-associated protein, is essential for brain development and autophagy. Proc Natl Acad Sci 2017; 114: E9308–17.

Kawabe H, Sakisaka T, Yasumi M, Shingai T, Izumi G, Nagano F, et al. A novel rabconnectin-3-binding protein that directly binds a GDP/GTP exchange protein for Rab3A small G protein implicated in Ca(2+)-dependent exocytosis of neurotransmitter. Genes Cells 2003; 8: 537–46.

Lieberman OJ, McGuirt AF, Tang G, Sulzer D. Roles for neuronal and glial autophagy in synaptic pruning during development. Neurobiol Dis 2019; 122: 49–63.

Liu X, Wu C, Li C, Boerwinkle E. dbNSFP v3.0: A one-stop database of functional predictions and annotations for human nonsynonymous and splice-site SNVs. Hum Mutat 2016; 37: 235–41.

Maddirevula S, Alzahrani F, Al-Owain M, Al Muhaizea MA, Kayyali HR, AlHashem A, et al. Autozygome and high throughput confirmation of disease genes candidacy. Genet Med 2018; 0: 1–7.

Marsh D, Dragich JM. Autophagy in mammalian neurodevelopment and implications for childhood neurological disorders. Neurosci Lett 2019; 697: 29–33.

Merkulova M, Păunescu TG, Azroyan A, Marshansky V, Breton S, Brown D. Mapping the H(+) (V)-ATPase interactome: identification of proteins involved in trafficking, folding, assembly and phosphorylation. Sci Rep 2015; 5: 14827.

Nagano F, Kawabe H, Nakanishi H, Shinohara M, Deguchi-Tawarada M, Takeuchi M, et al. Rabconnectin-3, a novel protein that binds both GDP/GTP exchange protein and GTPase-activating protein for Rab3 small G protein family. J Biol Chem 2002; 277: 9629–32.

Saitsu H, Nishimura T, Muramatsu K, Kodera H, Kumada S, Sugai K, et al. De novo mutations in the autophagy gene WDR45 cause static encephalopathy of childhood with neurodegeneration in adulthood. Nat Genet 2013; 45: 445–9.

Sethi N, Yan Y, Quek D, Schupbach T, Kang Y. Rabconnectin-3 is a functional regulator of mammalian notch signaling. J Biol Chem 2010; 285: 34757–64.

Shehata M, Matsumura H, Okubo-Suzuki R, Ohkawa N, Inokuchi K. Neuronal stimulation induces autophagy in hippocampal neurons that is involved in AMPA receptor degradation after chemical long-term depression. J Neurosci 2012; 32: 10413–22.

Sobreira N, Schiettecatte F, Valle D, Hamosh A. GeneMatcher: a matching tool for connecting investigators with an interest in the same gene. Hum Mutat 2015; 36: 928–30.

Steriade M, Amzica F, Contreras D. Cortical and thalamic cellular correlates of electroencephalographic burst-suppression. Electroencephalogr Clin Neurophysiol 1994; 90: 1–16.

Tang G, Gudsnuk K, Kuo S-H, Cotrina ML, Rosoklija G, Sosunov A, et al. Loss of mTOR-dependent macroautophagy causes autistic-like synaptic pruning deficits. Neuron 2014; 83: 1131–43.

Tata BK, Harbulot C, Csaba Z, Peineau S, Jacquier S, De Roux N. Rabconnectin-3α is required for the morphological maturation of GnRH neurons and kisspeptin responsiveness. Sci Rep 2017; 7: 1–12.

Tata B, Huijbregts L, Jacquier S, Csaba Z, Genin E, Meyer V, et al. Haploinsufficiency of Dmxl2, encoding a synaptic protein, causes infertility associated with a loss of GnRH neurons in mouse. PLoS Biol 2014; 12: e1001952.

Teinert J, Behne R, Wimmer M, Ebrahimi-Fakhari D. Novel insights into the clinical and molecular spectrum of congenital disorders of autophagy. J Inherit Metab Dis 2019. doi: 10.1002/jimd.12084.

Tuttle AM, Hoffman TL, Schilling TF. Rabconnectin-3a regulates vesicle endocytosis and canonical Wnt signaling in zebrafish neural crest migration. PLoS Biol 2014; 12: e1001852.

Vijayan V, Verstreken P. Autophagy in the presynaptic compartment in health and disease. J Cell Biol 2017; 216: 1895–906.

Wang Z, Miao G, Xue X, Guo X, Yuan C, Wang Z, et al. The Vici syndrome protein EPG5 is a Rab7 effector that determines the fusion specificity of autophagosomes with late endosomes/lysosomes. Mol Cell 2016; 63: 781–95.

Xiong HY, Alipanahi B, Lee LJ, Bretschneider H, Merico D, Yuen RKC, et al. RNA splicing. The human splicing code reveals new insights into the genetic determinants of disease. Science 2015; 347: 1254806.

Yan Y, Denef N, Schüpbach T. The vacuolar proton pump, V-ATPase, is required for notch signaling and endosomal trafficking in Drosophila. Dev Cell 2009; 17: 387–402.